

# An approach to Physics Based Single Photon Vision System Design

Yizhou Lu\*, Trevor Seets\*, Felipe Gutierrez-Barragan†, Ehsan Ahmadi\* and Andreas Velten\*‡

\*Department of Electrical and Computer Engineering, University of Wisconsin-Madison, Madison, United States

†Department of Computer Sciences, University of Wisconsin-Madison, Madison, United States

‡Department of Biostatistics and Medical Informatics, University of Wisconsin-Madison, Madison, United States

**Abstract**—The design of the camera and optical measurement is a crucial part of optimizing machine vision systems. However, camera designs are usually optimized to produce human-interpretable images. Moreover, camera optimization typically makes the assumption of additive noise, while modern optical imaging systems are mainly affected by photon noise which is not additive. Previous studies have highlighted the fundamental effect of the noise model on the outcome of the design process in the context of coded single-pixel and compressed sensing cameras.

In addition to the exact noise model, the nature of the data encountered and the vision task fundamentally affect the optimal hardware design. This means that a camera or compressed sensing code that is optimal for capturing images is almost certainly not optimal for any downstream vision task. In this work, we used a simple end-to-end model on a single-pixel camera to study the effects of the noise model for different vision tasks. We demonstrate the importance of incorporating non-linear noise features in optimizing even the simplest vision systems.

**Index Terms**—Optical coding, photon noise, single-pixel-camera, data-driven prior, optical-neural-networks

## I. INTRODUCTION

While we can mass-produce optical components of increasing complexity, most vision hardware still closely mimics the optics of the human eye to create easily interpretable images. In this approach, the lens projects an image that is then post-processed to extract patterns. However, more generalized vision systems can perform alternative measurements that may be more perceptually meaningful than simply producing images. Designing such systems requires a collaborative effort to integrate hardware and digital processing algorithms while considering the appropriate noise model. The significance of this approach is particularly illustrated by the single-pixel camera in this context.

The single pixel camera uses the concept of optical coding, or multiplexing, which involves projecting an image onto a mask and collecting the transmitted light with a large sensor pixel. The system can potentially achieve an improved signal-to-noise ratio (SNR) and higher light throughput by coding compared to point-by-point measurements [1]. In this context, a measurement vector  $\mathbf{y}$  is formed from a set of measured photon counts, with the corresponding masks vectorized as rows of the sensing matrix  $M$ . Ignoring the noise, coding can be represented as

$$\mathbf{y} = M\mathbf{x}, \quad (1)$$

where  $\mathbf{x}$  is the signal vector. Decoding refers to the process of recovering the initial signal  $\mathbf{x}$  from  $\mathbf{y}$ . The recovery quality of  $\mathbf{x}$  is significantly dependent on the conditioning of  $M$  and the light throughput of  $M$  [1]. Suboptimal  $M$  have the potential to significantly degrade the performance of the vision system during the recovery process, as highlighted by Mitra et al. [1].

While a greater light throughput, or a lower noise level, can improve recovery, the improper choice of the noise model can also give rise to a suboptimal coding at specific noise levels. Coding design is often performed under the assumption of signal-independent additive Gaussian Noise (AGN) which arises from imperfect sensors. With advances in sensor design, even the sensor noise of low-end camera sensors has been reduced to a few photons per pixel. This reduction is significant enough so that nonadditive photon noise becomes the primary noise factor in the vast majority of imaging applications [2]. Photon noise follows a super-Poissonian distribution [3]. For passive cameras operated with incoherent ambient light the noise can usually be approximated as Poissonian.

The transition from AGN to more realistic photon noise fundamentally alters the designs of vision systems. For example, although single-pixel cameras with random masks provide performance advantages under AGN, they do not outperform a simple sequential scan when dealing with Poisson noise [4]–[8]. Moreover, optimal coding designs under AGN conditions do not deliver optimal performance under Poisson noise at the same noise levels.

To address this issue, Mitra et al. [1] develop a method using data-driven priors to design optimized codes for image reconstructions. Their approach significantly improves the performance of coding under Poisson noise by designing measurements specifically targeting sparsity or compressibility in the data [1]. However, image recovery is typically not the ultimate goal for modern vision systems. Since vision tasks, such as classification, operate in embeddings created from images, their data should be inherently more compressible than their upstream imaging tasks, allowing for more effective measurement designs. To show this, we implement a simple end-to-end vision system that can be optimized under different noise assumptions. We illustrate why AGN is not suitable for optimizing coding under photon noise and show that a coding scheme optimized for a specific vision task and for the correct noise model can perform close to the optimal non-coding camera even when photon noise is present.

Our contributions are as listed.

- We introduce the methodology of Selective Sensing (SS), which encompasses coding techniques specifically designed to extract data-driven priors selectively for various downstream tasks.
- We provide an end-to-end vision model using classification as the performance metric, which is more perceptually meaningful than mean-squared-error (MSE), to optimize  $M$ .
- We propose a hybrid optimization method for non-differentiable Poisson noise that employs AGN with signal-dependent variance and the reparameterization trick to estimate gradients during training, while switching to Poisson noise in the testing stage for model assessment.

Our model is extendable to more general camera optics and different vision tasks in future work.

## II. RELATED WORK

**Coding under photon noise.** In coded imaging, Hadamard matrices are considered the optimal coding scheme for multiplexing [1], [2], [4], [9] in systems with only AGN, although this conclusion does not hold for photon noise [1]. In many recent projects, optimization efforts focus on algorithmic enhancements for reconstruction, often maintaining the use of random coding strategies [10]–[13], though this type of matrices are not recommended under photon noise [6], [8], [14]. Wuttig and Ratner, et al. [9], [15] introduced photon-noise-aware optimization techniques for coding matrices that outperform Hadamard in the presence of moderate signal-dependent noise. However, their analysis neglects the data priors, leading to suboptimal matrices for greater photon noise [1]. Additionally, attempts at matrix optimization focusing on minimal mutual coherence [16] do not adequately consider photon noise, as highlighted in this study.

**Feature Specific Imaging.** Feature-specific imaging (FSI) is a type of imaging system where sensing matrix  $M$  incorporates linear features of expected data [17], [18]. This approach can provide higher feature fidelity and lower detector count than conventional imaging, especially for applications that require relatively few features [17]–[19]. This technique can be viewed as a variant of compressed sensing, in which the sensing matrix is determined based on prior information [19]. However, current state-of-the-art FSI is explicitly designed for AGN rather than Poisson noise [19]. FSI can be regarded as a technique that leverages data driven priors, and Mitra et al. have asserted that employing data driven priors can enhance image recovery under Poisson noise [1]. Therefore, in our work, we underscore the promising prospects of extending feature-specific concepts to a broad spectrum of vision tasks under Poisson noise.

**End-to-end optimization.** This method jointly optimizes camera design and digital signal processing to achieve optimal overall performance [20]–[22]. In many previous projects, this idea was usually implemented without considering Poisson noise in cost functions [11], [22]–[28] or without optimizing masks with gradient incorporating Poisson distribution [11], [20], [29]–[33]. Rego et. al froze the sensing matrix as

a pinhole setting without optimizing it [30]. Wang et al. [32] successfully implemented a neural network model for handwritten number classification on an optical device with limited photon budget, demonstrating the potential for AI-assisted optimization of coding schemes. However, Poisson noise was considered only in model testing where the most robust model was picked among a set of different initialization seeds [32]. Xu et al. [33] examined the robustness of the proposed neural network model to Poisson noise; however, the training process does not explicitly incorporate the gradients affected by Poisson noise. As we see later, however, the correct noise model is essential to obtain an optimal or near-optimal optical design. Our contribution in this area is developing a noise-aware training approach within a neural network model to find globally optimal masks under Poisson noise. Although our approach also employs data-driven priors, which is similar to that of Mitra et al., our research extends beyond simple image reconstruction to address a wider spectrum of vision tasks and investigates task-specific optimization techniques on optical hardware.

## III. BACKGROUND

### A. Single Pixel Camera

The single-pixel camera shown in Fig. 1 is a popular example of coding, and serves as the primary example in this project. It employs a rapid single-pixel detector in conjunction with a Digital Micromirror Device (DMD) to sequentially multiplex a sensing matrix by modulating various patterns on the DMD [1]. Its measurement process mathematically follows the Eq. 1. Here,  $\mathbf{x} \in \mathbb{R}^{N \times 1}$  is the image representation of the field of view (FOV), which consists of  $N$  pixels, and is measured by linear projections or masks,  $M \in \mathbb{R}^{m \times N}$  to attain corresponding flux levels or photon counts,  $\mathbf{y} \in \mathbb{R}^{m \times 1}$  [6]. Physically,  $M$  can be implemented on the DMD by directing or blocking different parts of the incoming light from  $\mathbf{x}$  [34] and averaging them on sensors that digitize the detected flux levels or photon counts  $\mathbf{y}$ . If the sensing matrix  $M$  is full-rank, the  $\mathbf{x}$  can be reconstructed by  $M^{-1}\mathbf{y}$ . However, even when  $m < N$ , we can still recover the  $\mathbf{x}$  via compressed sensing. While Hadamard matrices are considered effective for  $M$ , their suitability diminishes in the presence of data-dependent noise [1], [4]. In this work, we will study the performance of this camera for different choices of  $M$  under different noise models.

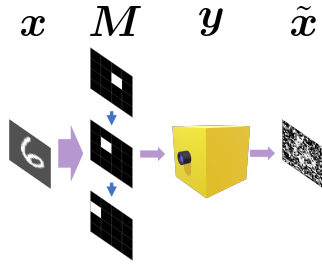
### B. Selection of Sensing Matrix

Eq. 1 is the foundational equation for a single-pixel camera. Based on it, we distinguish different types of  $M$  below for reference and guidance.

#### 1) Coding Types:

- **Raster scan** entails a pixel-wise scanning approach where photon counts for all pixels are sequentially measured [11]. Mathematically, the sensing matrix  $M = I$ , an identity matrix.
- **Impulse imaging** (conventional imaging) entails an ideal camera that simultaneously captures all elements in the

(a) Direct Measurement Strategy: Raster Scan



(b) Computational Imaging (CI) Strategy: Basis Scan

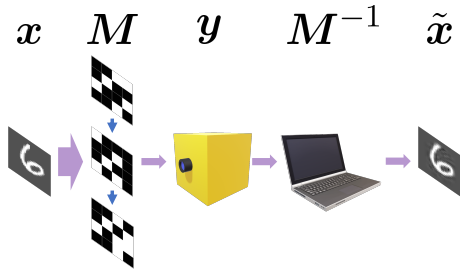


Fig. 1:  $x$ : object,  $M$ : masks of coding,  $y$ : counted photon numbers at the sensor,  $M^{-1}$ : reconstruction operator,  $\tilde{x}$ : reconstructed object. (a) Only one pixel (white) is scanned in each measurement, and the measured data requires no reconstruction. (b) The sum of all white pixels is measured in each measurement and it requires a decoding step to reconstruct the field of view.

measurements,  $y$ . The key feature of this system is its use of a pixel array sensor instead of a single-pixel sensor. This allows for the detection of all incoming photons, whereas the raster scan only collects a small fraction, specifically  $\frac{1}{N}$  when the field of view  $x$  consists of  $N$  pixels. Therefore, the sensing matrix assumes the form  $M = NI$  where  $I$  is an identity matrix. This technique sets a benchmark akin to a gold standard, serving as an upper limit for the CI performance and an indicator of the noise level for comparison.

- **Non-Selective Codes** refer to coding schemes that uncorrelated with the inherent compressibility or statistical attributes of a specific dataset. Examples include widely used codes like Hadamard patterns and Rademacher Random codes. This category also includes truncated Hadamard patterns that use low-frequency components of the complete Hadamard basis.
- **Selective Codes** encompass coding schemes selectively learn the significant features from training data to effectively capture sparse data representations. When under AGN, FSI finds data specific codes through Principal Component Analysis (PCA).

## 2) Vision Tasks:

- **Signal Reconstruction (Null-prior/No Compression)**: In tasks involving classic imaging, a null-prior is assumed,

and there is no compression during measurements. The rank of the measurement matrix  $M$  is required to be equal to  $N$ , the number of pixels in the  $x$  and no prior or bias should be introduced through  $M$ .

- **Computational Imaging (Weak-prior/Some Compression)**: In this kind of task, a weak-prior assumption is made. This idea, which focuses on image reconstruction, is based on prior knowledge, such as signals being sparse in some linear space, with noise concentrated in the high-frequency domain. One example in this category is compressed sensing.
- **Vision (Strong-prior/Much Compression)**: Many computer vision tasks involve a strong prior, enabling substantial compression during measurements. Activation of the main feature directly by  $M$  is possible if some of its components resemble  $x$ . In these tasks, a few measurements are often sufficient with a strong prior derived from training data. Our focus is on optimizing the codes in this scenario.

## C. Constraints of sensing matrices

The implementation of the sensing matrix  $M$  usually involves the following constraining factors.

- 1) **Flux-preserving** [6]. The single-pixel camera model involves the allocation of available photons among masks, as discussed in [18]. It is important to ensure that the mask basis  $M$  does not produce additional photons through improper entries [18]. Mathematically,  $\sup \sum_{i=1}^m M_{ij} = 1, \forall j \in \{1, 2, \dots, N\}$  [18].
- 2) **Positivity-preserving** [6]. It is not possible to physically implement negative values for masks  $M$ , as demonstrated in [6], [18]. In this project, we used the dual-rail approach as outlined in the work of Neifeld et al. where the positive and negative entries of a mask give rise to two separate measurements [18].

## D. Model under Noise

This project investigates two noise models. The first one is AGN related to dark current or read noise from imperfect sensor materials, which mainly originates from thermal vibrations of atoms at sensors. In this noise model, Eq. 1 becomes:

$$\tilde{y} = Mx + \epsilon, \quad (2)$$

where  $\epsilon \sim \mathcal{N}(0, \sigma^2 I)$ , and  $\sigma$  is the standard deviation. The other noise model is photon noise, which arises from the statistical nature of photons [35]. In most prior research, this is approximated as Poisson noise, and the measurement equations associated with this noise model typically follow a Poisson distribution:

$$\tilde{y} \sim \text{Poisson}(Mx)$$

$$\Pr(\tilde{y}_i = k) = \frac{y_i^k \exp(-y_i)}{k!}, \quad (3)$$

where  $y_i = \sum_{j=1}^N M_{ij} x_j$  [6]. It should be noted that the constraint 2 in Eq. 3 prohibits negative entries in  $M$ . While Poisson noise is the best way to approximate photon noise

at this stage, its limitations for this project extend beyond just physical inaccuracies. The nonlinearity of photon noise adds complexities to the design and optimization of affected systems, and the use of Poisson random functions eliminates gradients, making it difficult to optimize the hardware components in the end-to-end model. To address these shortcomings, this project focuses on the signal dependency of photon noise and adopts a quasi-classical model known as MLGAUSS that uses a Gaussian variable with mean-variance equivalence [36], formulated as

$$\begin{cases} \tilde{\mathbf{y}} = \mathbf{M}\mathbf{x} + \mathbf{J}, \\ \mathbf{J} = (\mathbf{M}\mathbf{x})^{\circ\frac{1}{2}} \odot \boldsymbol{\epsilon}, \\ \boldsymbol{\epsilon} \sim \mathcal{N}(0, \mathbf{I}), \end{cases} \quad (4)$$

It substitutes conventional Poisson approximations whenever a gradient computation is required, yet the term "Poisson" is retained for consistency with other classical models involving no hardware optimization, facilitating straightforward comparisons. While this approach represents an alternative version of approximated photon noise besides Poisson noise, it is utilized exclusively during model training. For model testing, all models employ the Poisson noise model, as gradient computation is no longer necessary.

## IV. METHODS

### A. Model Configuration

All coding strategies in this project for classification tasks share the same fundamental model structure, as illustrated in Fig. 2. In this project, we apply our model to handwritten number classification with the MNIST dataset and classification of hyperspectral data. To classify handwritten numbers using optical devices with limited photon budget, we built a PyTorch-based pipeline consisting of a *scanner* module including  $\mathbf{M}$  and a noise generator to simulate the acquisition of  $\tilde{\mathbf{y}}$  described in Eq. 2 and Eq. 3, and a *classifier* module classifying the measured objects by  $\tilde{\mathbf{y}}$ . For the classification task, we utilized a two-hidden layer artificial neural network (ANN) with 40 and 128 nodes, serving as the primary model. To prevent overfitting and enhance generalizability, we applied dropout after each hidden layer, followed by a rectified linear unit (ReLU) activation layer. Once operational, this model can serve various purposes, such as object classification and signal recovery. For instance, it can process images of handwritten numbers, providing the likelihood of each image corresponding to a specific number by cross-entropy loss. Furthermore, the classifier can function as a decoder to recover the input image by MSE loss, which is adopted in section IV-B.

During model training, the scanner computes the photon counts with noise and then transmits these data to the classifier. The noise is sampled from a predefined noise distribution and varies across epochs. Once the loss has been computed, the gradient descent is used to optimize the classifier parameters. In addition, we propose an end-to-end optimization model called Optical Neural Networks (ONN). What sets the ONN apart from other coding schemes is the learnable  $\mathbf{M}$  which is not predefined or fixed. In other words, backpropagation

is extended to the scanner, allowing the simultaneous optimization of the masks and the classifier under different noise models. This approach offers distinct advantages compared to traditional methods, which typically optimize the classifier independently of the scanner or optimize the scanner without the appropriate noise model.

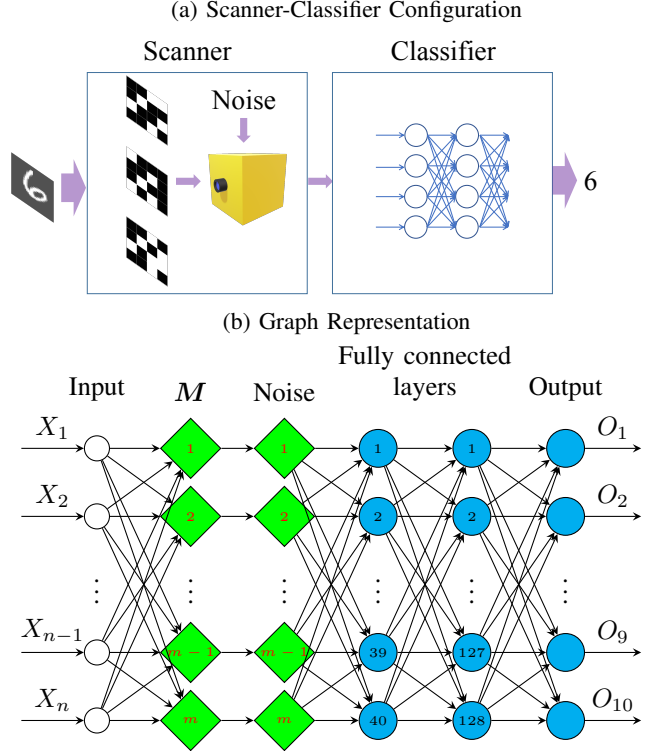


Fig. 2: (a) the general configuration of scanner-classifier networks. (b) the node-level architecture of our scanner (green diamonds)-classifier (blue circles) network. Noise is implemented after the sensing matrix  $\mathbf{M}$ . Different from other coding schemes, ONN has a trainable scanner where  $\mathbf{M}$  is not fixed and can be optimized by the gradient of the classifier.

*ONN Optimization under Poisson Noise:* Optimizing the scanner can be challenging, as the Poisson random function typically lacks a gradient. We employ the reparameterized-Gaussian model mentioned in section III-D to address this limitation. This approach enables us to employ the PyTorch built-in reparameterization method, that is, `rsample`, and optimize the scanner more effectively under Poisson noise. During the training stages, variance plays a crucial role in the gradient computation, marking a significant difference compared to training under conventional Poisson models.

### B. Model Validation

To validate the proposed ONN model, we apply it to non-compressible signal reconstruction tasks where the correct solution is known. Previous theoretical studies have shown that multiplexing, such as Hadamard coding, is not recommended under Poisson noise for greater MSE [31] and lower SNR [4] compared to raster scan. In this project, we compare

Hadamard and raster coding under both AGN and Poisson noise conditions to see whether the ONN model reaches similar conclusions.

Given the universality of reconstruction algorithms, it is imperative that the input data vector  $\mathbf{x}$ , is not compressible. Hence, we generate  $\mathbf{x}$  by randomly sampling from the uniform distribution  $U(0, 1)$ . Throughout the optimization process, these inputs are regenerated 10 times, thereby introducing additional randomization and reducing compressibility. The output is the reconstructed  $\mathbf{x}$ , with MSE between the input and the output serving as the loss function. The simulations are conducted with a total of  $1 \times 10^2$  photons which is used to rescale the  $\mathbf{x}$  to simulate a short exposure, given that AGN and Poisson noise behave more differently under low-light conditions. We initialize the masks  $\mathbf{M}$  with an  $N \times N$  identity matrix and a  $\{0, 1\}$  Hadamard matrix, respectively, and optimize them until the model reports constant losses.

Fig. 3a displays the first 6 optimized masks from both initial matrices generated by the ONN model under both AGN and Poisson noise. Specifically, it tends to open more pixels to enhance light throughput under AGN, but adheres to the RS mode under Poisson noise. Fig. 3b provides a more detailed visualization of the optimized masks by presenting the distribution of their entries. The x-axis represents the values in the masks, while the y-axis shows the total number of entries within a specific range. This observation aligns with the reconstruction results, where the RS performed modestly under AGN but considerably better under Poisson noise. Gradients incorporating these two noise models during the training process lead mask optimization in very different directions. From this example, we can see that it is not appropriate to design a coding system under AGN and then apply it to Poisson noise data.

### C. Computer Simulated Experiments

In this section, we present two distinct classification tasks. Initially, we evaluated the effectiveness of various coding schemes using the MNIST dataset, focusing on their performance in number recognition. Subsequently, we extend the evaluation to hyperspectral data, examining the adaptability and efficacy of the coding schemes in this different domain.

1) *MNIST Simulated Data Preparation:* The MNIST dataset, which consists of handwritten digits ranging from 0 to 9, has a default size of 28 by 28 pixels [37]. To align the data with Hadamard matrices, we add black pixels to the edges of the images and resize them to 32 by 32 pixels [37]. Subsequently, we rescale the pixel values from the original range of  $[0, 1]$  to  $[0.3, 1]$ . This rescaling introduces non-zero Poisson noise to the black regions, which has variance proportional to the expected photon counts.

We evaluate our proposed model through simulations incorporating both AGN and Poisson noise models, using varying exposure times to generate results at different noise levels. We also test all compressible strategies, varying the total number of masks but fixing the total exposure time, and define a metric called compression ratio as the ratio of the number of masks to the number of pixels [38]. For RS and HB, this ratio is

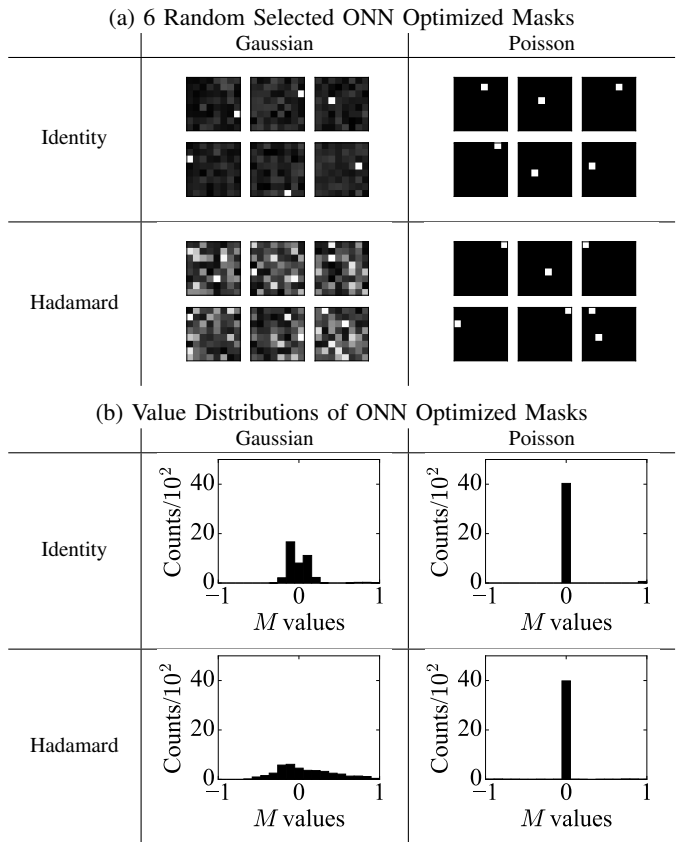


Fig. 3: Optimizations on the matrix  $\mathbf{M}$ , initialized with identity and Hadamard matrices, are explored under both AGN and Poisson noise. (a) shows some optimized masks and (b) shows the distributions of all entries in  $\mathbf{M}$  after optimization. While  $\mathbf{M}$  demonstrates a preference for strategies with higher light throughput under AGN, it consistently leans toward the raster scan strategy under Poisson noise, irrespective of the initialization matrices. The challenge arises from the non-convex nature of this optimization problem, making it difficult to converge perfectly to the identity matrix. Nevertheless, this deviation underscores fundamental distinctions in optimizing masks under these distinct noise models.

restricted to 1.00, while the rest are evaluated over values in  $\mathcal{C}_R \in \{0.01, 0.04, 0.09, 0.16, 0.25, 0.36, 0.49, 0.64, 0.81, 1.00\}$  so that  $\mathbf{M}$  of each coding scheme is not restricted to being full-rank. The final comparison involves only the best results among all compression ratios for each strategy. Unlike pre-defined masks used by other strategies, the initial masks for ONN can affect performance in the presence of noise. We therefore initialized its masks with the PCA components from the training data.

2) *Spectral Datasets and Performance Evaluation:* We use the Indian Pines dataset [39], acquired through AVIRIS on June 12, 1992, covering the Purdue University Agronomy farm and surrounding areas. With  $145 \times 145$  pixels and 224 spectral bands (0.4 to 2.5  $\mu\text{m}$ ) per pixel, this dataset offers a comprehensive view of this area. Fig. 4a illustrates 16 classes in Indian Pines, along with their counts and semantic labeling

of the ground truth. It features a representation of band-12 for all pixels. Fig. 4b shows the relative intensity of the selected classes from the spectrum data, providing a concise overview of their differences.

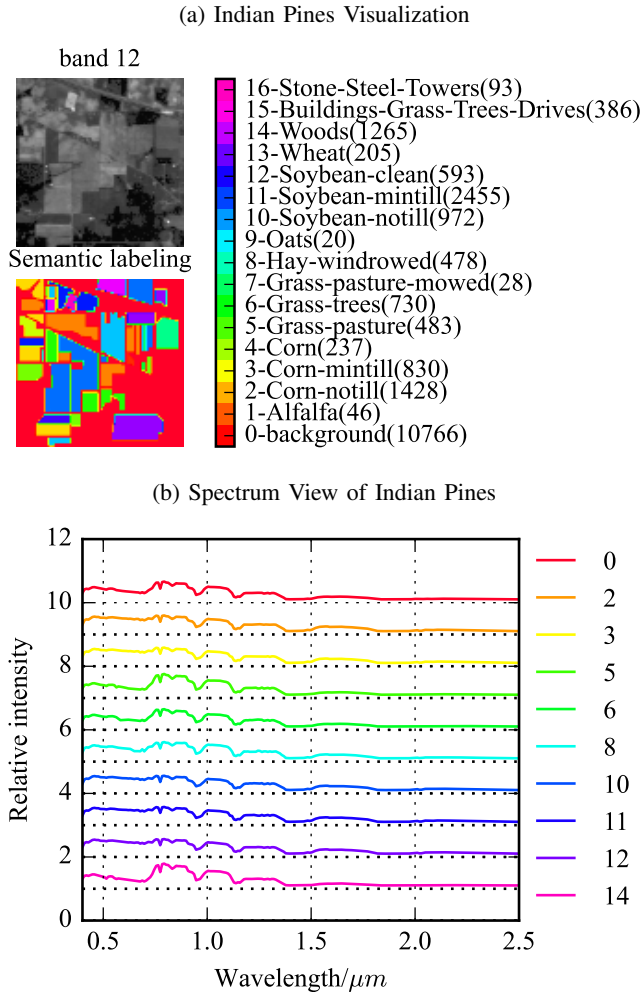


Fig. 4: (a) Visualization of the Indian Pines dataset using Band 12 from the entire spectrum (top-left). The bottom-left figure represents classes with distinctive colors as specified in the legend, which includes class labels and their respective counts [39]. (b) Average spectrum for each selected class in the Indian Pines dataset. Classes with data entries fewer than 400 are excluded. Baselines are shown as dashed horizontal lines under each spectrum.

In the experiment, spectral data vectors, extracted as arrays from each pixel, are zero-padded from 224 to 256 in length for Hadamard mask alignment and rescaled to  $[0, 1]$ . It undergoes processing using the modified scanner-classifier module illustrated in Fig. 2. The classifier is simplified into a single fully connected layer with 1478 neurons, using the default architecture provided by `scikit-learn` during the preproject testing phase which gives an 86% classification rate without any coding or noise. The ONN classification layers are adjusted to accommodate input data subsets, each containing

400 entries per class. Classes with fewer than 400 entries are omitted to maintain an unbiased input.

Model performance is evaluated using average classification rates from five independent tests. Each test involves a random 90%-10% training-validation split of the dataset. Training continues until the validation rate plateaued or declined, with the highest validation rate representing the upper bound for each test. The final performance metric is the average of the five maximum validation rates, ensuring a reliable and accurate assessment of the model.

#### D. Hardware Experiments

To further support our conclusions, we conduct an experiment in addition to simulations. As shown in Fig. 5, the experiment utilizes a DMD (digital micromirror device), specifically the DLP 7000 model from Texas Instruments, and a PMT (photomultiplier tube) from PicoQuant, specifically the PMA Series. The experimental setup involves both hardware-end data acquisition and software-end classifier training. Handwritten number images are displayed on a monitor, captured by this vision system, and subsequently identified according to the depicted numbers.

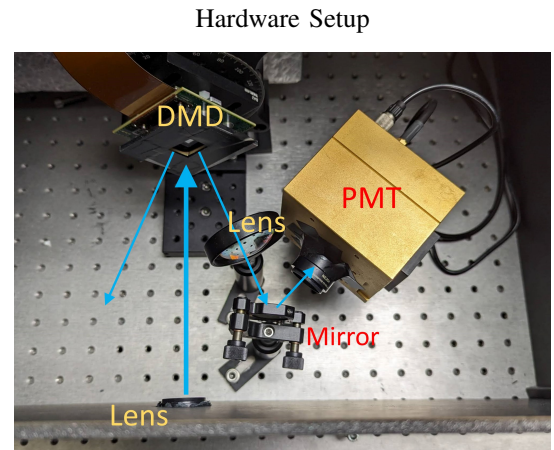


Fig. 5: Experimental configuration of the single-pixel camera: The light path is illustrated by the blue arrows in the diagram. Specifically, our setup utilizes only one branch reflected by the DMD.

To ensure that the classifier is properly trained using the PMT data, we perform a transformation  $g(\cdot)$  that incorporates illumination correction and calibration of the MNIST images  $\mathbf{X}$  to match what the PMT would actually "observe",  $\mathbf{X}^g$ , during data acquisition. Mathematically, this transformation can be described as  $\mathbf{X}^g = g(\mathbf{X})$ . This step aims at reducing the model inconsistency between optimizing the sensing matrices  $\mathbf{M}$  and classifiers with digital data on a computer and testing the models with the data acquired from the experiments. Specifically, we perform a raster scan of a sample from  $\mathbf{X}_s$ , a random subset from  $\mathbf{X}$ , with each mask exposed for 1 second. The light intensity is adjusted to ensure that the brightest pixel generated approximately 1000 photon counts per second. The data  $\mathbf{X}_s^g$  captured during this experiment is then reshaped into a 32 by 32 image, as shown in Fig. 6, and  $g(\cdot)$  is then

determined. Applying the transformation to digital data yields  $\mathbf{X}^g$ , which is then fed into models featuring various coding schemes for performance evaluation.

Following the generation of mask pattern sequences, they are uploaded onto the DMD to capture data, represented as  $\tilde{\mathbf{y}}$ . Our test set consists of ten handwritten images, each of which appears exactly once during the experiment. To control the noise level in the data, we varied lengths of random intervals throughout the 1-second exposure time for each mask. For instance, considering only the photons detected in the first 0.5-second interval, we effectively double the noise level. By preserving the arrival times of all photons, we can systematically adjust the level of noise in the acquired data.

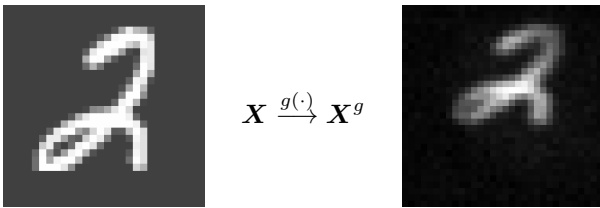


Fig. 6: Raw image  $\mathbf{X}$  (left) VS PMT-observed image  $\mathbf{X}^g$

## V. RESULTS

### A. Classification Rates on Simulated Experiment Data

Fig. 7 displays the classification performance of different coding schemes. Since Poisson noise is signal dependent and AGN is not, comparing the performance under both models is not straight forward. To provide a common metric for both models, the x-axis is the log-scaled MSE of impulse imaging (II) with varying exposure times. This MSE is the gold standard in this project and serves as a metric to measure the noise level for both AGN and Poisson noise models. The y-axis represents the validation set's classification rate. A good way to understand the results is to consider the performance of different schemes in relation to the curves for II and RS. Measurements for each of the schemes can be created as some subset of an II measurement. Thus it should not be possible for any coded single pixel system to perform better than II. RS is the trivial code allowing simple implementation that also transmits the least amount of light. We expect it to perform poorly and any code with worse performance than it seems hard to justify as a useful scheme. We evaluate the codes by noting how they perform within these two extremes. The results presented in the figure demonstrate that as expected II consistently achieves the highest performance. In the presence of AGN, all coding schemes exhibit significant improvements over RS and in many cases provide adequate performance. This is because under Gaussian noise, projection from a captured basis into a basis of sparsity where the classifier operates can be done without a significant noise penalty. Moreover, for the classification task at hand, SS measurement techniques such as PCA and ONN, can yield further improvements in classification performance. Notably, the ONN approach produces results that are nearly as good as the II approach, while reducing the number of pixels on the sensor from several thousands to one.

However, when dealing with Poisson-distributed measured data, the effectiveness of non-selective coding is no longer superior to that of RS. This aligns with the findings of Harwit et al. [4], which discourage the adoption of coding for Poisson noise. Despite this, there is still potential for performance improvement by utilizing SS methods such as PCA and ONN.

### B. Classification Performances on Hardware Experiment Data

In our experiments, the collected data take the form of a series of timestamps recording the photon arrival time. During data collection, both RS and HB uses 1024 masks, while TH and HB employ the same measured data, but TH uses only the first 92 measurements for compression purposes. Similarly, PCA and ONN utilizes 92 masks. Physical measurements take one second per mask for all strategies. To generate data with higher noise levels from the raw data, we randomly select intervals within the 1-second span and count the total number of photons within them. Since ONN and PCA have only 92 masks, the maximum exposure time is set to 92 seconds. To ensure a fair comparison, we compute the interval length for each strategy as  $\frac{\tau}{m}$ , where  $\tau$  represents the total exposure time under investigation, and  $m$  denotes the number of masks used for each strategy.

Fig. 8 displays the classification rates achieved on the experimental data. The x-axis shows the exposure time, and the y-axis represents the classification rates of the models. Although there may be discrepancies between software training and hardware data acquisition, the ONN models outperform other coding schemes across all noise levels. However, the figure reveals some unexpected phenomena. Firstly, the HB strategy outperforms the RS for short exposure times, which is not observed in the simulations. This phenomenon may have arisen due to the dark counts in the PMT, a signal-independent noise that has about 40-80 counts per second under our lab condition. Secondly, TH achieves better classification performances than PCA when the exposure time is short. This result is due to the use of unneeded PCA masks since the compression ratio was not optimized as it was in the simulation. To verify, we conduct simulations and obtain Fig. 9 by fixing the total number of photons at  $10^5$  and varying the compression ratio under Poisson noise. This figure shows that PCA method can perform worse than the TH if an improper compression ratio is chosen. Hence, PCA strategy requires careful estimation of the noise level to avoid improper compression ratios. Notably, ONN demonstrates enhanced stability and robustness when confronted with this challenge. This flexibility in application allows for broader use of the ONN beyond its specific training conditions, increasing its potential impact and utility in real-world scenarios.

### C. Simulated Experiment on Hyper-Spectral Data

Fig. 10 depicts the classification rates for the Indian Pines dataset under different light levels. Consistent with the findings on the MNIST dataset, all coding schemes enhance classification performance under Gaussian noise. However, under Poisson noise, only SS demonstrates comparable efficacy to

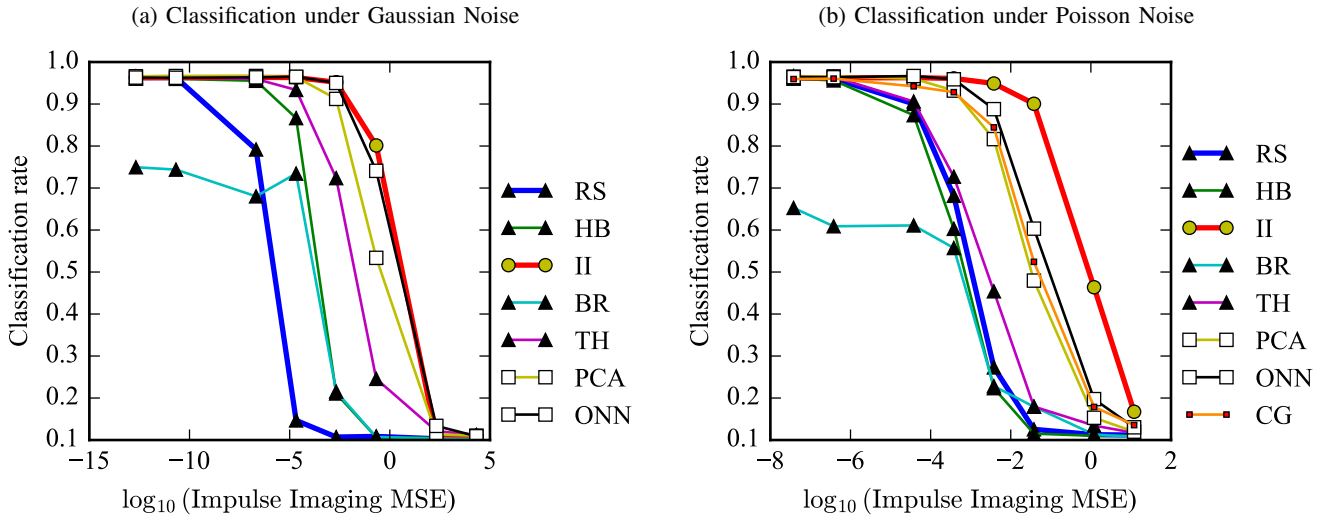


Fig. 7: Classification rates on **simulated data**. RS: Raster basis. HB: Hadamard basis. II: Impulse imaging. BR: Binary random basis. TH: Low Frequency Truncated Hadamard basis. PCA: PCA basis. ONN: Optical Neural Networks. CG: control group. Selective strategies are marked by  $\square$  and non-selective strategies are marked by  $\blacktriangle$ . (a) RS is the worst but using other non-selective coding strategies can improve the performance under the AGN. (b) Among all non-selective strategies, only selective strategies can significantly improve the performance under Poisson noise. The CG employs the optimized masks under the AGN and trains the software classifier under Poisson noise. Its performance is worse than the ONN.

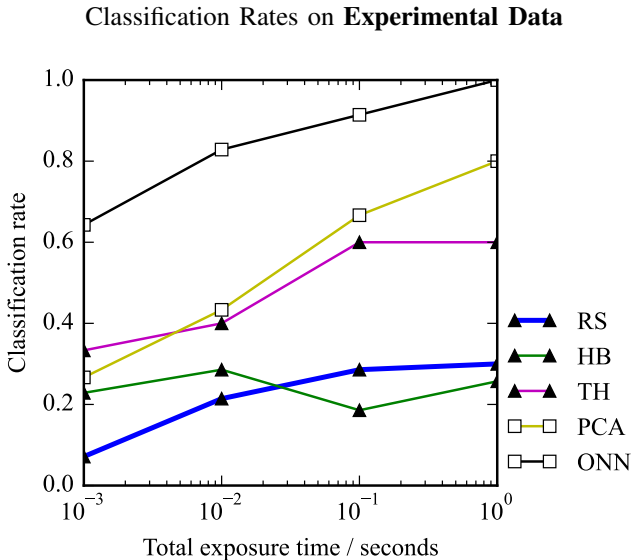


Fig. 8: RS: Raster basis. HB: Hadamard basis. TH: Low Frequency Truncated Hadamard basis. PCA: PCA basis. ONN: Optical Neural Networks. Selective strategies are marked by  $\square$  and non-selective strategies are marked by  $\blacktriangle$ . ONN is in general the best strategies given the experimental data.

impulse imaging. This outcome implies that SS holds promise for advancement in hyperspectral data applications.

## VI. DISCUSSION AND LIMITATIONS

Our paper highlights the challenges of computational imaging under Poisson noise and its impact on algorithms based

on the AGN noise assumption. We find that for compressible measurements, and especially tasks that involve direct feature extraction instead of signal reconstruction, a Selective Sensing approach using task-based optimized codes provides a viable coding solution. Through simulations and experiments, we demonstrate the feasibility of Selective Sensing and its promising classification performance on the MNIST handwritten number dataset. It is also robust in application scenarios with difficult-to-estimate noise levels. Our ONN method represents a method that can generate these selective measurements. Furthermore, Selective Sensing motivates the development of optical ANNs or ANNs with optical layers to globally optimize imaging systems.

In computational imaging, coding typically involves measuring analog flux through a coding projection such as mask in our case. However, this analog model neglects inherent Poisson noise in real measurements, leading to counterintuitive coding behaviors. Viewing the system as measuring photons through different codes provides more intuitive insights. Both total number of photons and the amount of information about their original pixels matter. For instance, a photon measured through a mask with open pixels carries less scene information than one through a raster mask, where each photon can be uniquely assigned to a pixel. This challenge becomes critical in the era of low-noise, photon-counting cameras dominated by Poisson noise. This issue is significant as the projection process studied in specific coding experiments is integral to the design of any camera, where high-dimensional scene data is projected into a lower-dimensional sensor space encountering Poisson noise for subsequent scene inferences.

Despite the promising results of our project, there are



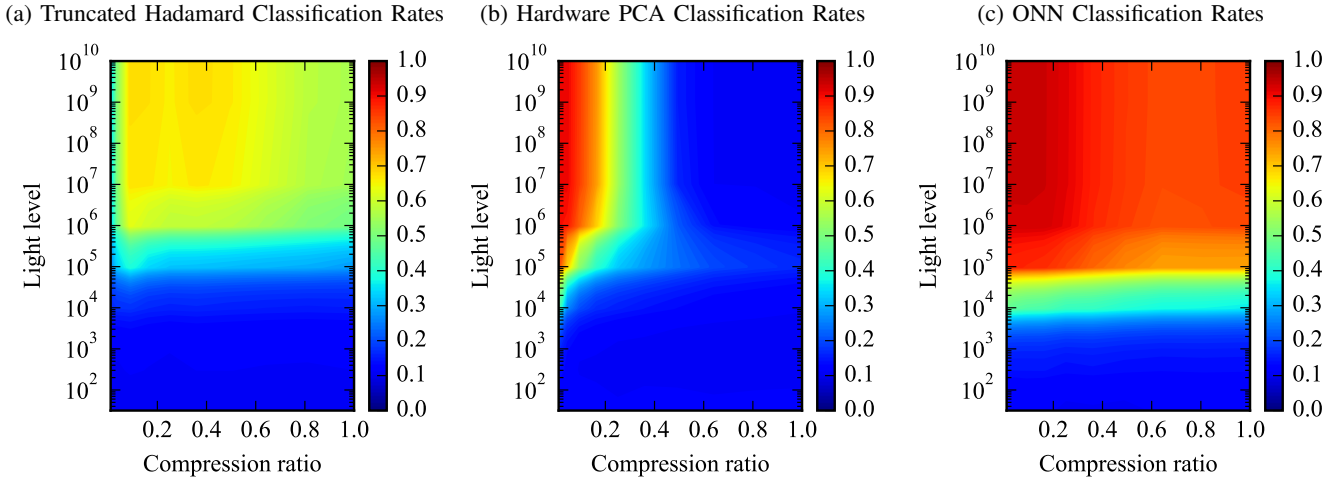


Fig. 9: Classification rates on simulated data regarding compression ratios and light levels. The models are trained under Poisson noise using a light level of  $10^5$  photons and subsequently tested under different light levels. It is observed that hardware PCA performance deteriorates when the compression ratio is not properly chosen, whereas the Truncated Hadamard and ONN models exhibit greater robustness in such scenarios.

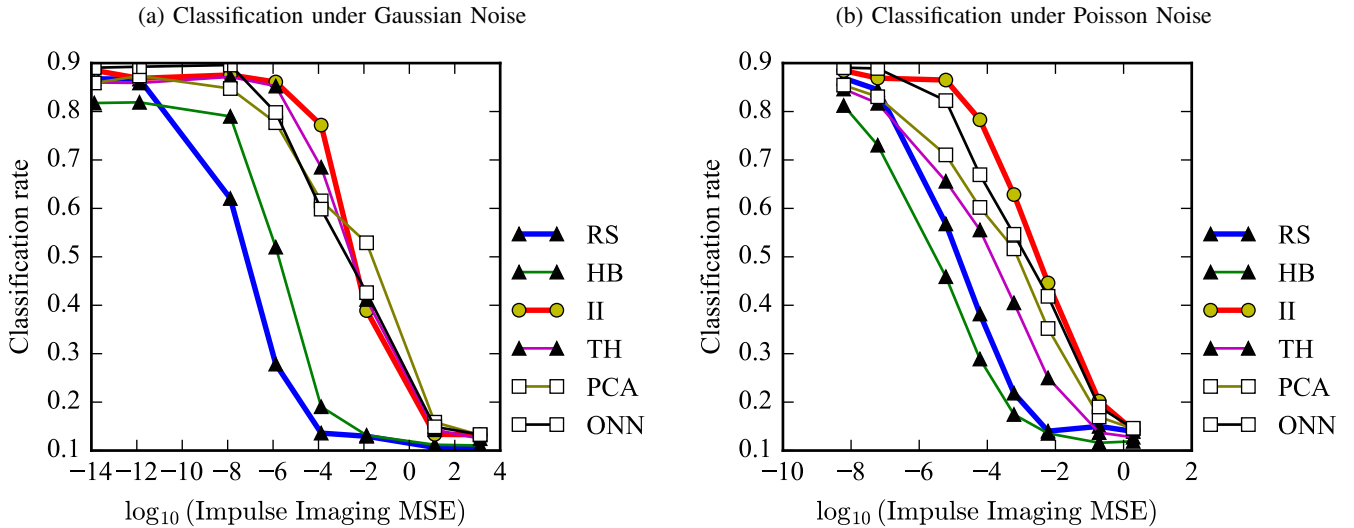


Fig. 10: Classification rates of Indian Pines dataset varying light level. RS: Raster basis. HB: Hadamard basis. II: Impulse imaging. TH: Low Frequency Truncated Hadamard basis. PCA: PCA basis. ONN: Optical Neural Networks.

some limitations that must be acknowledged. First, we used a noise model where the variance equals the mean and applied reparameterization to approximate the actual photon noise at the sensor. This approach offers a valid alternative to Poisson noise, which is also just an approximation. Second, our test set consisted of only 10 numbers, which may not provide a comprehensive evaluation of the model's performance. These limitations highlight the need for further improvements in the optimization of the ONN model, such as using more advanced optimization methods and larger sets of experimental data. Our

work highlights the importance of the integration of imaging hardware and signal processing. In single photon accurate imaging systems, comprehensibility and sparsity of the data can be exploited to far greater effect during the measurement, as opposed to post processing.

## REFERENCES

- [1] K. Mitra, O. Cossairt, and A. Veeraraghavan, "Can we beat hadamard multiplexing? data driven design and analysis for computational imaging systems," in *2014 IEEE International Conference on Computational Photography (ICCP)*. IEEE, 2014, pp. 1–9.
- [2] O. Cossairt, M. Gupta, and S. K. Nayar, "When does computational imaging improve performance?" *IEEE transactions on image processing*, vol. 22, no. 2, pp. 447–458, 2012.
- [3] L. Mandel, "Fluctuations of photon beams: the distribution of the photoelectrons," *Proceedings of the Physical Society*, vol. 74, no. 3, p. 233, 1959.
- [4] M. Harwit and N. J. A. Sloane, *Hadamard Transform Optics*. Academic Press, 1979.
- [5] R. D. Swift, R. B. Wattson, J. A. Decker, R. Paganetti, and M. Harwit, "Hadamard transform imager and imaging spectrometer," *Applied optics*, vol. 15, no. 6, pp. 1595–1609, 1976.
- [6] M. Raginsky, R. M. Willett, Z. T. Harmany, and R. F. Marcia, "Compressed sensing performance bounds under poisson noise," *IEEE Transactions on Signal Processing*, vol. 58, no. 8, pp. 3990–4002, 2010.
- [7] C. Scotté, F. Galland, and H. Rigneault, "Photon-noise: is a single-pixel camera better than point scanning? a signal-to-noise ratio analysis for hadamard and cosine positive modulation," *Journal of Physics: Photonics*, vol. 5, no. 3, p. 035003, 2023.
- [8] W. Van den Broek, B. W. Reed, A. Béché, A. Velazco, J. Verbeeck, and C. T. Koch, "Various compressed sensing setups evaluated against shannon sampling under constraint of constant illumination," *IEEE Transactions on Computational Imaging*, vol. 5, no. 3, pp. 502–514, 2019.
- [9] A. Wuttig, "Optimal transformations for optical multiplex measurements in the presence of photon noise," *Appl. Opt.*, vol. 44, no. 14, pp. 2710–2719, May 2005. [Online]. Available: <https://opg.optica.org/ao/abstract.cfm?URI=ao-44-14-2710>
- [10] D. Shin, J. H. Shapiro, and V. K. Goyal, "Performance analysis of low-flux least-squares single-pixel imaging," *IEEE Signal Processing Letters*, vol. 23, no. 12, pp. 1756–1760, 2016.
- [11] G. M. Gibson, S. D. Johnson, and M. J. Padgett, "Single-pixel imaging 12 years on: a review," *Optics express*, vol. 28, no. 19, pp. 28 190–28 208, 2020.
- [12] A. Liutkus, D. Martina, S. Popoff, G. Chardon, O. Katz, G. Lerosey, S. Gigan, L. Daudet, and I. Carron, "Imaging with nature: Compressive imaging using a multiply scattering medium," *Scientific reports*, vol. 4, no. 1, p. 5552, 2014.
- [13] E. J. Candès and M. B. Wakin, "An introduction to compressive sampling," *IEEE signal processing magazine*, vol. 25, no. 2, pp. 21–30, 2008.
- [14] R. Willett and M. Raginsky, "Poisson compressed sensing," *Defense Applications of Signal Processing*, 2011.
- [15] N. Ratner, Y. Y. Schechner, and F. Goldberg, "Optimal multiplexed sensing: bounds, conditions and a graph theory link," *Optics express*, vol. 15, no. 25, pp. 17 072–17 092, 2007.
- [16] M. Mordechay and Y. Y. Schechner, "Matrix optimization for poisson compressed sensing," in *2014 IEEE Global Conference on Signal and Information Processing (GlobalSIP)*. IEEE, 2014, pp. 684–688.
- [17] M. Neifeld and P. Shankar, "Feature-specific imaging," *Applied optics*, vol. 42, pp. 3379–89, 07 2003.
- [18] H. S. Pal and M. A. Neifeld, "Multispectral principal component imaging," *Opt Express*, vol. 11, no. 18, pp. 2118–25, 2003 Sep 8.
- [19] A. Mahalanobis and M. Neifeld, "Optimizing measurements for feature-specific compressive sensing," *Applied Optics*, vol. 53, no. 26, pp. 6108–6118, 2014.
- [20] S. Diamond, V. Sitzmann, F. Julca-Aguilar, S. Boyd, G. Wetzstein, and F. Heide, "Dirty pixels: Towards end-to-end image processing and perception," *ACM Transactions on Graphics (TOG)*, vol. 40, no. 3, pp. 1–15, 2021.
- [21] K. Zhang, J. Hu, and W. Yang, "Deep compressed imaging via optimized pattern scanning," *Photonics research*, vol. 9, no. 3, pp. B57–B70, 2021.
- [22] R. Jacome, P. Gomez, and H. Arguello, "Middle output regularized end-to-end optimization for computational imaging," *Optica*, vol. 10, no. 11, pp. 1421–1431, 2023.
- [23] C. Hinojosa, J. C. Niebles, and H. Arguello, "Learning privacy-preserving optics for human pose estimation," in *Proceedings of the IEEE/CVF international conference on computer vision*, 2021, pp. 2573–2582.
- [24] X. Dun, H. Ikoma, G. Wetzstein, Z. Wang, X. Cheng, and Y. Peng, "Learned rotationally symmetric diffractive achromat for full-spectrum computational imaging," *Optica*, vol. 7, no. 8, pp. 913–922, 2020.
- [25] C. A. Metzler, H. Ikoma, Y. Peng, and G. Wetzstein, "Deep optics for single-shot high-dynamic-range imaging," in *Proceedings of the IEEE/CVF Conference on Computer Vision and Pattern Recognition*, 2020, pp. 1375–1385.
- [26] J. Chang and G. Wetzstein, "Deep optics for monocular depth estimation and 3d object detection," in *Proceedings of the IEEE/CVF International Conference on Computer Vision*, 2019, pp. 10 193–10 202.
- [27] E. Onzon, F. Mannan, and F. Heide, "Neural auto-exposure for high-dynamic range object detection," in *Proceedings of the IEEE/CVF conference on computer vision and pattern recognition*, 2021, pp. 7710–7720.
- [28] J. Spall, X. Guo, and A. I. Lvovsky, "Hybrid training of optical neural networks," *Optica*, vol. 9, no. 7, pp. 803–811, Jul 2022. [Online]. Available: <https://opg.optica.org/optica/abstract.cfm?URI=optica-9-7-803>
- [29] E. Tseng, A. Mosleh, F. Mannan, K. St-Arnaud, A. Sharma, Y. Peng, A. Braun, D. Nowrouzezahrai, J.-F. Lalonde, and F. Heide, "Differentiable compound optics and processing pipeline optimization for end-to-end camera design," *ACM Transactions on Graphics (TOG)*, vol. 40, no. 2, pp. 1–19, 2021.
- [30] J. D. Rego, H. Chen, S. Li, J. Gu, and S. Jayasuriya, "Deep camera obscura: an image restoration pipeline for pinhole photography," *Optics Express*, vol. 30, no. 15, pp. 27 214–27 235, 2022.
- [31] M. F. Duarte, M. A. Davenport, D. Takhar, J. N. Laska, T. Sun, K. F. Kelly, and R. G. Baraniuk, "Single-pixel imaging via compressive sampling," *IEEE Signal Processing Magazine*, vol. 25, no. 2, pp. 83–91, 2008.
- [32] T. Wang, S.-Y. Ma, L. G. Wright, T. Onodera, B. C. Richard, and P. L. McMahon, "An optical neural network using less than 1 photon per multiplication," *Nature Communications*, vol. 13, no. 1, p. 123, 2022.
- [33] Y. Xu, W. Liu, and K. F. Kelly, "Compressed domain image classification using a dynamic-rate neural network," *IEEE Access*, vol. 8, pp. 217 711–217 722, 2020.
- [34] R. Raskar, "Computational photography: Epsilon to coded photography," in *Emerging Trends in Visual Computing: LIX Fall Colloquium, ETVC 2008, Palaiseau, France, November 18-20, 2008. Revised Invited Papers*. Springer, 2009, pp. 238–253.
- [35] A. K. Boyat and B. K. Joshi, "A review paper: Noise models in digital image processing," *ArXiv*, vol. abs/1505.03489, 2015.
- [36] M. Selwood, "Coded aperture imaging: novel approaches to high-energy high-resolution laboratory imaging," Ph.D. dissertation, University of York, 2022.
- [37] Y. Lecun, L. Bottou, Y. Bengio, and P. Haffner, "Gradient-based learning applied to document recognition," *Proceedings of the IEEE*, vol. 86, no. 11, pp. 2278–2324, 1998.
- [38] R. Stojek, A. Pastuszczyk, P. Wróbel, and R. Kotyński, "Single pixel imaging at high pixel resolutions," *Optics Express*, vol. 30, no. 13, pp. 22 730–22 745, 2022.
- [39] M. F. Baumgardner, L. L. Biehl, and D. A. Landgrebe, "220 band aviris hyperspectral image data set: June 12, 1992 indian pine test site 3," Sep 2015. [Online]. Available: <https://purr.purdue.edu/publications/1947/1>

## ACKNOWLEDGMENT

The authors would like to thank Dr. Rebecca Willet for her invaluable assistance in refining the problem statement and providing support for our conclusions during the course of this research. Additionally, the authors would like to express gratitude to Dr. Sebastian Bauer for his guidance in understanding the mathematical aspects of this problem at its early stages. This work is supported by the National Science Foundation (1846884) and the Air Force Office for Scientific Research (FA9550-21-1-0341).